International Journal for Modern Trends in Science and Technology
Volume 12, Issue 04, pages 730-741.
ISSN: 2455-3778 online
Available online at: http://www.ijmtst.com/vol12issue04.html
DOI: https://doi.org/10.5281/zenodo.19567139

Design of an ANN-Assisted Adaptive Speed Controller for a Position-Sensorless PMBLDC Motor Drive with Regenerative Braking for LEV Applications

Dr. P. Lakshman Naik, R.Dhana Mahesh, I.lavaraju, K.kavya

Department of Electrical and Electronics Engineering, Vasireddy Venkatadri Institute of Technology, Pedakakani, Namburu, Guntur, India.

To Cite this Article
Dr. P. Lakshman Naik, R.Dhana Mahesh, I.lavaraju & K.kavya (2026). Design of an ANN-Assisted Adaptive Speed Controller for a Position-Sensorless PMBLDC Motor Drive with Regenerative Braking for LEV Applications. International Journal for Modern Trends in Science and Technology, 12(04), 730-741. https://doi.org/10.5281/zenodo.19567139

Article Info
Received: 16 March 2026; Revised: 06 April 2026; Accepted: 10 April 2026.

KEYWORDS

PMBLDC motor, ANN, sensorless control, adaptive speed control, regenerative braking, LEV applications

ABSTRACT

Light Electric Vehicles require high efficiency, compact design, and reliable motor drive systems with precise speed control and energy recovery capability. This paper presents the design and implementation of an ANN assisted adaptive speed controller for a position sensorless Permanent Magnet Brushless DC motor drive integrated with regenerative braking. The proposed system eliminates the need for mechanical position sensors by employing a back EMF based estimation technique, thereby reducing cost and improving system reliability. To address the challenges of nonlinearities, parameter variations, and external load disturbances in PMBLDC drives, an Artificial Neural Network is incorporated in the speed control loop. The ANN controller is trained to adaptively tune control signals, resulting in improved speed tracking accuracy, reduced steady state error, and enhanced dynamic response compared to conventional controllers. In addition, an adaptive delay compensation mechanism is employed to mitigate estimation delays inherent in sensorless operation. The regenerative braking scheme is designed to recover kinetic energy during deceleration and feed it back to the energy source, thereby improving overall system efficiency, which is essential for LEV applications. The effectiveness of the proposed control strategy is validated through simulation and experimental results, demonstrating superior performance in terms of speed regulation, robustness, and energy efficiency under varying operating conditions.

1. INTRODUCTION

The growing demand for environmentally friendly transportation has significantly accelerated the development of Light Electric Vehicles (LEVs) in recent years. LEVs have gained wide attention because of their compact size, low operating cost, reduced emissions, and suitability for urban transportation. In such applications, the selection of an efficient and reliable motor drive system is of great importance, since the overall performance of the vehicle is strongly dependent on the quality of speed control, dynamic response, and energy utilization [1], [2]. Among the various motor options available for LEVs, the Permanent Magnet Brushless DC (PMBLDC) motor has emerged as one of the most preferred choices due to its high efficiency, high torque density, compact structure, simple maintenance, and superior controllability [3], [4]. PMBLDC motors are particularly attractive for LEV applications because they provide improved efficiency over a wide speed range and possess better thermal performance compared to conventional brushed DC motors. Their electronic commutation mechanism eliminates brush wear and reduces maintenance requirements, which is a major advantage in modern transportation systems [5], [6]. However, achieving precise speed control in PMBLDC motor drives remains a challenging task because of system nonlinearities, rapid load variations, inverter switching effects, and parameter uncertainties arising from temperature change, magnetic saturation, and mechanical disturbances [7], [8]. These issues become even more critical in LEV applications, where stable operation, quick acceleration, smooth deceleration, and efficient energy management are essential. Traditionally, rotor position sensors such as Hall sensors, optical encoders, and resolvers have been employed in PMBLDC motor drives to determine rotor position for proper commutation and control. Although these sensors provide accurate position information, their use increases system cost, size, and complexity, while also reducing overall reliability due to sensor failures, wiring issues, and environmental sensitivity [9], [10]. In LEV applications, where compactness, robustness, and low cost are important design considerations, the elimination of mechanical position sensors is highly desirable. This has motivated extensive research on position sensorless control techniques for PMBLDC motors [11], [12]. Among the sensorless control approaches, back electromotive force based estimation methods are widely adopted because of their simple implementation and relatively good accuracy at medium and high speeds. These methods estimate rotor position by analyzing the zero crossing or waveform characteristics of the back EMF generated in the stator windings [13], [14]. However, sensorless estimation based on back EMF suffers from several limitations, particularly under low speed operation and transient conditions. Estimation delays, signal distortion, noise, and parameter mismatches can reduce commutation accuracy and deteriorate the dynamic performance of the drive system [15], [16]. Therefore, effective delay compensation and adaptive estimation techniques are necessary to improve the robustness of position sensorless PMBLDC drives. To enhance speed regulation performance in the presence of nonlinearities and uncertainties, intelligent control techniques have attracted significant attention in motor drive applications. Among them, Artificial Neural Networks (ANNs) have emerged as a powerful tool because of their capability to approximate nonlinear functions, learn complex system behavior, and adapt to varying operating conditions [17], [18]. Unlike conventional proportional integral or proportional integral derivative controllers, ANN based controllers can provide better dynamic performance under parameter variations and load disturbances without requiring an exact mathematical model of the system [19], [20]. This makes ANN based control highly suitable for PMBLDC motor drives used in LEVs, where operating conditions can change rapidly during start up, acceleration, climbing, braking, and varying payload conditions. ANN assisted adaptive speed controllers have been reported to improve reference speed tracking, reduce steady state error, minimize overshoot, and enhance disturbance rejection in various electric drive applications [21], [22]. By incorporating learning capability into the control loop, the controller can adjust its output according to changes in motor characteristics and load demand. In addition, combining ANN based speed control with sensorless position estimation can significantly improve the overall reliability and efficiency of the motor drive system. Nevertheless, the performance of such a combined approach depends on the quality of estimation algorithms, adaptation strategy, and delay compensation mechanism [23]. Another important requirement in LEV applications is efficient

energy utilization. Since the driving range of LEVs is limited by battery capacity, recovering kinetic energy during braking is highly beneficial. Regenerative braking is an effective technique that converts the kinetic energy of the motor and vehicle during deceleration into electrical energy and feeds it back to the battery or energy storage unit [24]. This not only improves energy efficiency and extends battery operating time, but also reduces mechanical brake wear and enhances the overall sustainability of the vehicle drive system [25]. However, the implementation of regenerative braking in a PMBLDC motor drive requires coordinated control of inverter switching, speed response, and energy flow to ensure smooth braking and stable operation. In this work, an ANN assisted adaptive speed controller is proposed for a position sensorless PMBLDC motor drive with regenerative braking intended for LEV applications. The proposed system employs a back EMF based sensorless estimation method to eliminate the need for mechanical position sensors, thereby reducing cost and improving system reliability. An adaptive delay compensation mechanism is incorporated to reduce the effect of commutation delay associated with sensorless operation. Furthermore, an ANN based speed controller is designed to improve speed tracking performance, reduce steady state error, and provide robustness against load disturbances and parameter variations. The regenerative braking strategy is integrated into the drive system to recover energy during deceleration and enhance overall drive efficiency. The proposed approach aims to provide an efficient, compact, and intelligent motor drive solution suitable for modern LEVs. By combining sensorless control, ANN based adaptive speed regulation, and regenerative braking capability, the system is expected to achieve improved dynamic performance, better reliability, and higher energy efficiency compared to conventional drive structures. The effectiveness of the proposed configuration can be evaluated through simulation and experimental validation under varying operating conditions.

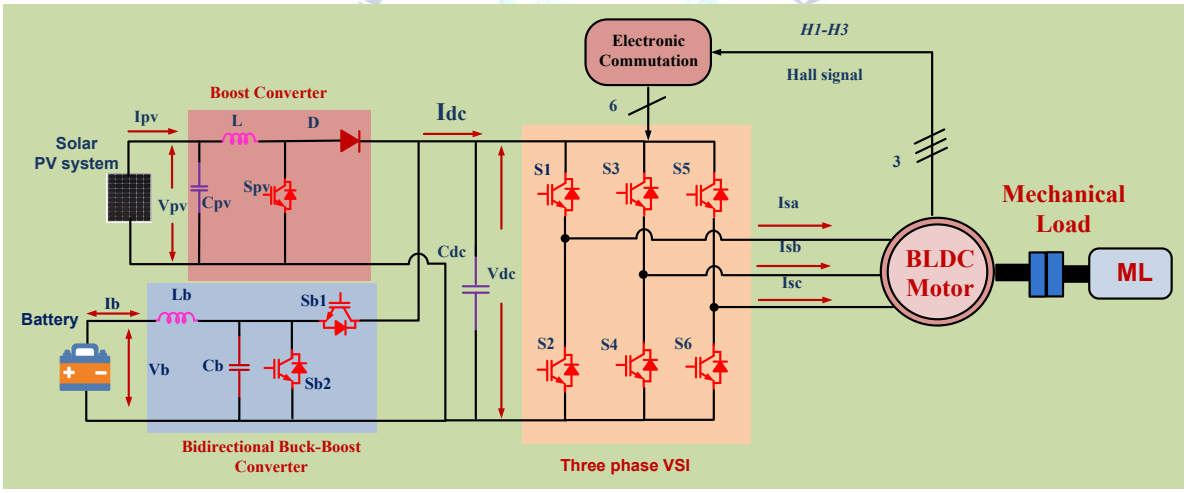

Fig. 1. Architecture of renewable based EVs charging station.

II. SYSTEM CONFIGURATION

As seen in Figure 1, the suggested setup includes a bidirectional power flow capability Permanent Magnet Brushless DC (PMBLDC) motor drive that is coupled with solar photovoltaic (PV) technology. The PV system is linked to the DC connection via a boost converter and serves as the main energy source. The Maximum Power Point Tracking (MPPT) algorithm controls this converter to manage the PV output voltage and guarantee maximum power extraction under fluctuating solar irradiation circumstances. The DC connection is linked to a battery energy storage system by a bidirectional buck-boost converter. Power from the photovoltaic source, stored in the battery, and transferred to the motor load efficiently using this converter's regulated charging and discharging capabilities. As PV production surpasses load demand, the surplus energy is stored in the battery. Conversely, when PV output is low, the battery provides power to keep the system running continuously. A capacitor-supported DC link supplies a three-phase Voltage Source Inverter (VSI) with a constant voltage. To drive the PMBLDC motor, the VSI transforms DC power into the three-phase AC supply that is necessary. Electronic commutation based on Hall

sensor signals controls the inverter switching; these signals advise the correct phase excitation of the rotor based on their location. A PMBLDC motor's speed is modulated by an ANN-based controller while it is linked to a mechanical load. Reliable performance in a wide range of operating situations, enhanced dynamic responsiveness, and decreased steady-state error are all guarantees of the controller. As a whole, the system allows for more effective use of renewable energy, more steady motor functioning, and better power management.

III. MODELING AND DESIGNING OF PROPOSED SYSTEM CONFIGURATION

A. Solar PV system

The single diode model effectively represents the behavior of a solar cell under varying temperature and solar irradiance conditions. When sunlight strikes the solar cell, a photo-generated current Iph is produced, which is directly proportional to the incident irradiance and slightly influenced by temperature variations. The model incorporates key parameters such as series resistance Rs, which accounts for internal resistive losses, and shunt resistance Rsh, which represents leakage currents within the cell. The diode in the model represents the p–n junction, capturing recombination losses that occur during operation. The output current I of the solar cell is determined by subtracting the diode and leakage currents from the photo-generated current, while also considering voltage drops across the internal resistances. Due to the nonlinear nature of this relationship, the governing equation must be solved iteratively for accurate analysis and design. By adjusting the operating voltage V, the solar cell can operate at different points along its current–voltage (I–V) characteristic curve. At the extremes, the current is zero under open-circuit conditions, while the voltage becomes zero during short-circuit conditions. Between these two limits lies the Maximum Power Point (MPP), which represents the optimal operating condition where the product of current and voltage is maximized. To ensure that the solar cell consistently operates near this point despite fluctuations in irradiance and temperature, Maximum Power Point Tracking (MPPT) techniques such as Perturb and Observe or Incremental Conductance are employed. These methods dynamically adjust the duty cycle of the DC–DC converter or the load conditions to extract maximum available power.

Overall, the single diode model serves as a reliable and widely used approach for analyzing and designing photovoltaic systems. It enables engineers to predict system performance under varying environmental conditions and to optimize the design of power electronic converters and energy management systems for efficient energy harvesting.

a. Single Diode Model of a PV Cell

Many PV modules and solar cells employ the single diode model to depict their electrical behavior, which captures their nonlinear current-voltage (I-V) properties.

1. Equivalent Circuit: A current source Iph in parallel with a diode (with saturation current I0), series resistance Rs, and shunt resistance Rsh.

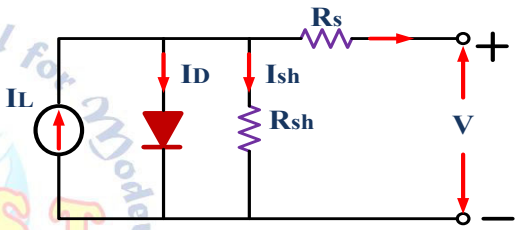

Fig. 2 equivalent model of PV solar.

2. Output Current Equation:

$$I_{ph} - I_0\left(e^{\frac{q(V+IR_S)}{nkT}-1}\right) - \frac{V+IR_S}{R_{sh}} \qquad (1)$$

Where:

- I = output current (A)
- V = output voltage (V)
- Iph = photo-generated current (A)
- I0 = diode saturation current (A)
- q = electron charge 1.602×10−19 C)
- n = diode ideality factor (typically 1 to 2)
- k = Boltzmann constant 1.381×10−23 J/K
- T = cell temperature (Kelvin)
- Rs = series resistance (Ω)
- Rsh = shunt resistance (Ω)

3. Photo-generated current Iph:

$$= \left[I_{sc} + K_i\left(T - T_{ref}\right)\right] \times \frac{G}{G_{ref}} \qquad (2)$$

Where:

- Isc = short-circuit current at reference temperature
- Ki = temperature coefficient of current (A/°C)
- Tref = reference temperature (usually 25°C or 298 K)
- G = solar irradiance (W/m²)
- Gref = reference irradiance (1000 W/m²)

4. Diode Saturation Current I0:

$$I_0 = I_{0_{ref}} \left(\frac{T}{T_{ref}}\right)^3 \exp\left(\frac{qE_g}{nk}\left(\frac{1}{T_{ref}} - \frac{1}{T}\right)\right) \quad (3)$$

Where:

- I0ref = diode saturation current at Tref
- Eg = bandgap energy of the semiconductor (eV)

5. Open-circuit voltage Voc:

$$V_{oc} = \frac{nkT}{q} In\left(\frac{I_{ph}}{I_0} + 1\right) \quad (4)$$

B. Solar PV boost Converter

As shown in Figure 3, a boost converter, a kind of DC-DC converter, may increase the output voltage from a lower input voltage. Its constituent parts are an inductor (L), a switch (usually a MOSFET), a diode (D), and an output capacitor (C). The voltage from the PV panel may be sent via the inductor after the power is turned on, as the MOSFET switch is closed. Instead of the diode, which can't conduct current because of its reverse bias, the energy is stored by the inductor's magnetic field. When the switch is turned off, the MOSFET opens, causing the inductor's magnetic field to diminish and the energy to be released. After passing through the diode, current multiplies the input voltage as it travels from the inductor to the output capacitor and load. If you want to charge batteries or power loads efficiently, you need to make sure the output voltage is higher than the input voltage.

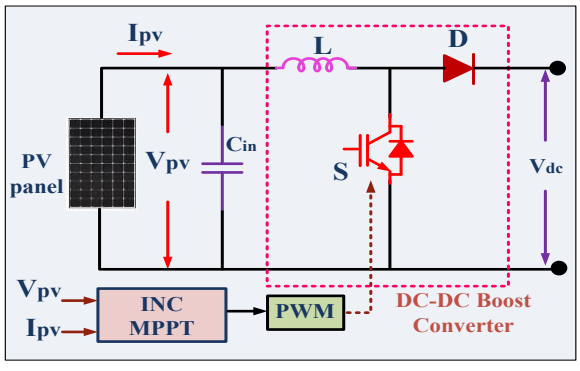

Fig. 3 solar PV INC MPPT DC-DC boost converter

1. Output Voltage of Boost Converter

$$V_o = \frac{V_{in}}{1-D} \quad (5)$$

Where: Vo: Output voltage, Vin: PV input voltage, D: Duty cycle (0 < D < 1)

2. Inductor Value (L)

$$L = \frac{V_{in} \cdot D}{f_s \cdot \Delta I_L} \quad (6)$$

Where:

- fs: Switching frequency (Hz)
- ΔIL: Inductor ripple current (A), usually 20–40% of Iin

3. Output Capacitor Value (C)

$$C = \frac{I_o \cdot D}{f_s \cdot \Delta V_o} \quad (7)$$

Where:

- Io: Output current (A)
- ΔVo: Acceptable output voltage ripple (V)

C. MPPT Control

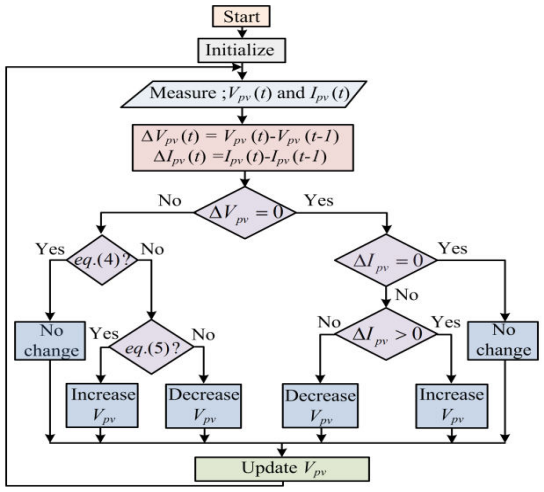

Fig. 4. INC MPPT control

Fig. 4 depicts the solar PV array's greatest power point technique. It generates a voltage reference (V*pv) that is the same as the MPP voltage of the PV array.

At the MPP,

$$\frac{dP_{PV}}{dV_{PV}} = 0 \quad (8)$$

$$\frac{d(V_{PV}I_{PV})}{dV_{PV}} = I_{PV} + V_{PV}\frac{dI_{PV}}{dV_{PV}} = 0 \quad (9)$$

$$\frac{dI_{PV}}{dV_{PV}} = -\frac{I_{PV}}{V_{PV}} \quad (10)$$

Right side displays PV array instantaneous conductance.

Conditions of INC MPPT control:

$$\frac{dI_{PV}}{dV_{PV}} = -\frac{I_{PV}}{V_{PV}}\left(\frac{dP_{PV}}{dV_{PV}} = 0, \text{at MPP}\right) \quad (11)$$

$$\frac{dI_{PV}}{dV_{PV}} > -\frac{I_{PV}}{V_{PV}}\left(\frac{dP_{PV}}{dV_{PVg}} > 0, \text{at left of MPP}\right) \quad (12)$$

$$\frac{dI_{PV}}{dV_{PV}} < -\frac{I_{PV}}{V_{PV}}\left(\frac{dP_{PV}}{dV_{PV}} < 0, \textit{at right of MPP}\right) \quad (13)$$

According to the circumstances, the disturbance arises in the PV array's voltage, which is used to monitor the array's maximum power point.

D. Bidirectional Buck-Boost Converter for Battery Energy Storage System

An essential component of any microgrid, the bidirectional buck-boost converter controls the flow of electricity from the BESS to the DC bus. Charging and draining the battery are both made possible by this converter, which guarantees a steady supply of power for EV charging. As seen in Figure 5, the converter may be used to charge the battery by stepping down the DC bus voltage in buck mode, or to send power to the microgrid or electric vehicle load by stepping up the battery voltage in boost mode. To properly manage power flow, the control technique dynamically modifies the duty cycle. To further reduce voltage variations caused by intermittent renewable power sources, such as wind and solar, the converter aids in stabilizing the DC bus voltage. Longer battery life and greater system efficiency are the results of the energy management strategy's emphasis on appropriate charging and discharging cycles.

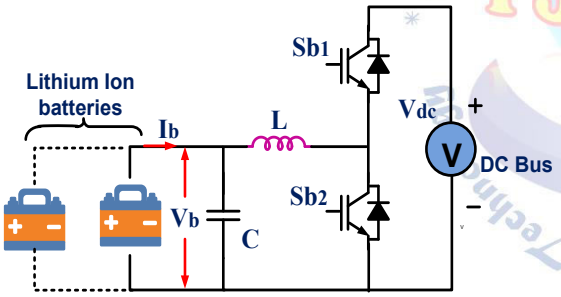

Fig.5 principle operation bidirectional dc-dc buck boost converter

1. Buck Mode (Battery Charging)

Output Voltage in Buck Mode:

$$V_b = D \cdot V_{dc} \quad (9)$$

Where: Vb = Battery voltage, Vdc = DC bus voltage, D = Duty cycle (0<D<1)

Inductor Current Ripple in Buck Mode:

$$\Delta I_L = \frac{(1-D)V_{dc}}{Lf_S} \quad (10)$$

Where: ΔIL = Inductor current ripple, L = Inductor value, fs = Switching frequency

2. Boost Mode (Battery Discharging)

Output Voltage in Boost Mode:

$$V_{dc} = \frac{V_b}{1-D} \quad (11)$$

Inductor Current Ripple in Boost Mode:

$$\Delta I_L = \frac{DV_b}{Lf_S} \quad (12)$$

E. Double-Loop Controller for EV Charging System

As seen in Figure 6, the control method for charging electric vehicles (EVs) utilizes a double-loop control system to guarantee safe, efficient, and reliable charging. The inner current loop controls the current going into the batteries, while the outside voltage loop keeps the DC bus voltage constant. In order to enhance dynamic performance and minimize steady-state error, a Proportional-Integral (PI) controller is utilized in both loops.

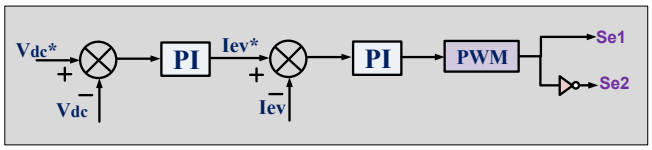

Fig. 6 double loop ev charging controller

1. Outer Voltage Loop: DC Bus Voltage Control

The outer voltage loop ensures the DC bus voltage (V_{dc}) remains stable and within the desired range. Since variations in EV charging loads and grid fluctuations affect the DC bus voltage, this loop provides a reference current (I_{ev}^*) for the inner current loop.

Error Signal Calculation:

$$e_v(t) = V_{dc}^* - V_{dC} \quad (13)$$

PI Controller Output (Reference EV Charging Current Iev∗

$$I_{ev}^*(t) = K_{Pv}e_v(t) + k_{iv}\int e_v(t)\,dt \quad (14)$$

Where: Iev∗= Reference charging current for the inner loop, Kpv= Proportional gain of voltage controller, Kiv= Integral gain of voltage controller

This reference current is then passed to the inner current loop for precise battery charging control.

2. Inner Current Loop: Battery Current Control

The inner current loop ensures the EV battery is charged with a smooth and regulated current to prevent over current issues and battery degradation. The PI controller in this loop generates the duty cycle for the DC-DC converter (buck or boost).

Error Signal Calculation:

$$e_i(t) = I_{ev}^* - I_{ev} \quad (15)$$

PI Controller Output (Duty Cycle Control)

$$D(t) = K_{Pi}e_i(t) + k_{ii}\int e_i(t)\,dt \quad (16)$$

Where: D = Duty cycle of the DC-DC converter, Kpi= Proportional gain of current controller, Kii= Integral gain of current controller

This duty cycle (D) is applied to the DC-DC converter, adjusting the output voltage and current to regulate battery charging.

IV. MODELING AND DESIGNING OF BLDC MOTOR

Electronically commutated stator windings, which generate electromagnetic torque, are the basis of the design and modeling of the Brushless DC (BLDC) motor. Instead of using brushes for commutation, BLDC motors utilize rotor position sensors (such Hall-effect sensors) and a three-phase inverter to precisely regulate the switching sequence, setting them apart from typical DC motors. To achieve maximum efficiency and minimum torque ripple, the motor's design has a permanent magnet rotor and stator windings organized in a trapezoidal back-EMF arrangement. Dynamic equations for stator voltage, current, back EMF, and torque production make up the BLDC motor's mathematical model, which is implemented in the MATLAB/Simulink environment. Feedback on the location of the rotors controls the inverter that drives the motor, enabling speed regulation and commutation in real time. Careful consideration is given to the needs of the application while selecting parameters such stator resistance, inductance, and the back EMF constant. A closed-loop control system is included into the simulation model to stabilize operation under different load circumstances and adjust the motor speed to the appropriate set point. The smart energy system's motor dynamics, efficiency, and performance may be precisely analyzed using this modeling technique.

A. Mathematical Designing of BLDC Motor

The electrical and mechanical behavior of the Brushless DC (BLDC) motor is described by a set of mathematical equations that are used in its construction. A permanent magnet rotor and a three-phase stator make up a BLDC motor. Commutation in BLDC motors is electronic and regulated by a three-phase inverter depending on the rotor position measured by Hall-effect sensors, unlike brushed DC motors.

The fundamental form of the phase voltage equation, which may be expressed for each phase as follows, is followed by the stator winding of the BLDC motor.

$$V_a = R \cdot i_a + L \cdot \frac{di_a}{dt} + e_a \quad (17)$$

$$V_b = R \cdot i_b + L \cdot \frac{di_b}{dt} + e_b \quad (18)$$

$$V_c = R \cdot i_c + L \cdot \frac{di_c}{dt} + e_c \quad (19)$$

Where: Va,Vb,Vc are the phase voltages, ia,ib,ic are the phase currents, R is the stator resistance per phase, L is the stator inductance per phase, ea,eb,ec are the back electromotive forces (EMF) of each phase

The back-EMF in each phase is dependent on the rotor position and speed, and is expressed as:

$$e_a = f_a(\theta) \cdot \omega \cdot k_e \quad (20)$$

$$e_b = f_b(\theta) \cdot \omega \cdot k_e \quad (21)$$

$$e_c = f_c(\theta) \cdot \omega \cdot k_e \quad (22)$$

Where: fa(θ),fb(θ),fc(θ) are the trapezoidal back-EMF waveforms as a function of rotor position θ, ω is the rotor speed in rad/s, Ke is the back-EMF constant

The electromagnetic torque generated by the motor is given by:

$$T_a = \frac{1}{\omega}(e_a i_a + e_b i_b + e_c i_c) \quad (23)$$

The mechanical equation of the motor governing its rotational dynamics is:

$$T_e - T_L = J \cdot \frac{d\omega}{dt} + B \cdot \omega \quad (24)$$

Where: TL is the load torque, J is the moment of inertia, B is the damping coefficient

The motor is typically controlled using a six-step (trapezoidal) commutation technique where each pair of inverter switches conducts for 120° electrical duration. Hall-effect sensors or sensorless estimation techniques are used to determine rotor position and enable appropriate switching sequences in the inverter.

V. DESIGNING OF ANN CONTROLLER FOR SPEED CONTROL OF BLDC MOTOR

By estimating the nonlinear control law between the speed error signals and the needed control action, the ANN controller is meant to manage the speed of the BLDC motor. By taking the role of the traditional controller and producing the reference control signal for the voltage source inverter, the artificial neural network (ANN) in the suggested system forces the motor speed to closely match the target reference speed. The controller employs a multi-layer network architecture to handle the speed error and its evolution; each layer applies a nonlinear activation function after a weighted summation. Due to this, tracking performance, steady-state error, and transient responsiveness are all improved, even when the load and the source are changed.

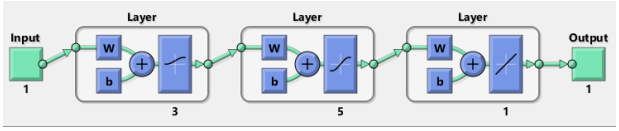

Figure 7: Structure of Neural Network

A. Actual Speed Measurement and Error Calculation

The ANN controller input is derived from the difference between the reference speed and the measured motor speed. The instantaneous speed error is expressed as

$$e(t) = \omega^*(t) - \omega(t) \quad (25)$$

where ω∗(t) is the reference speed of the BLDC motor, ω(t) is the actual measured motor speed, and e(t) is the instantaneous speed error.

The change in error is also considered as an additional input in order to capture the dynamic variation of the speed response:

$$\Delta e(t) = e(t) - e(t-1) \quad (26)$$

Hence, the ANN input vector is written as

$$x(t) = \begin{bmatrix} e(t) \\ \Delta e(t) \end{bmatrix} \quad (27)$$

This allows the controller to use both the present deviation and the trend of speed variation to predict the appropriate control action.

B. General ANN Mapping

The ANN approximates the nonlinear mapping between the input vector and the control output as

$$u(t) = f_{ANN}(x(t), w, b) \quad (28)$$

where u(t) is the artificial neural network's control output, x(t) is the input vector, W and b are the weight matrices and bias vectors, and fANN is the network's realized nonlinear mapping. It is possible to use the ANN output u(t) as the reference current, duty ratio, or control voltage for the VSI in BLDC motor speed control, depending on the technique used. To keep the motor running at the specified speed and regulate the inverter's functioning, it is used in this task to generate the necessary control signal.

C. Input to First Hidden Layer

Each neuron in the first hidden layer performs weighted summation of the inputs:

$$z_1 = W_1 x(t) + b_1 \quad (29)$$

where W1 is the weight matrix connecting the input layer to the first hidden layer and b1 is the corresponding bias vector.

The activation function used in the first hidden layer is the log-sigmoid function:

$$h_1 = f_1(z_1) = \log\text{sig}(z_1) = \frac{1}{1+e^{-z_1}} \quad (30)$$

The log-sigmoid function compresses the neuron output into the range [0,1], which is useful for smooth nonlinear mapping and normalized internal representation.

D. First Hidden Layer to Second Hidden Layer

The outputs of the first hidden layer are then combined in the second hidden layer according to

$$z_2 = W_2 h_1 + b_2 \quad (31)$$

The activation function in the second hidden layer is the tangent-sigmoid function:

$$h_2 = f_2(z_2) = \tan\text{sig}(z_2) = \frac{2}{1+e^{-2z_2}} - 1 \quad (32)$$

which is equivalent to the hyperbolic tangent function:

$$\tanh(z) = \frac{e^z - e^{-z}}{e^z + e^{-z}} \quad (33)$$

The tansig activation function produces outputs in the range [−1,+1]. Its symmetry about zero makes it suitable for representing both accelerating and decelerating control actions in BLDC motor speed regulation.

E. Output Layer

The output layer performs a linear combination of the second hidden layer outputs:

$$z_3 = W_3 h_2 + b_3 \quad (34)$$

A linear activation function is employed at the output layer:

$$u(t) = f_3(z_3) = purelin(z_3) = z_3 \quad (35)$$

This allows the ANN to generate an unbounded continuous control signal suitable for the inverter or motor drive controller.

F. Training Objective

The ANN parameters are adjusted by minimizing the mean squared error between the target control signal and the ANN output. The performance index is defined as

$$E = \frac{1}{N}\sum_{k=1}^{N}[T(k) - n(k)]^2 \quad (36)$$

where T(k) is the target control signal, u(k) is the ANN output, and NNN is the total number of training samples.

For BLDC speed control, the training data are generated from the motor drive under different operating conditions, including changes in speed reference, load torque, and DC-link voltage. Thus, the ANN learns the appropriate control action needed to maintain stable speed tracking.

E. Weight Update Rule

The network weights are updated using the Levenberg–Marquardt learning algorithm, expressed as

$$W^{new} = W^{old} - (J^T J + uI)^{-1} J^T e \quad (37)$$

where J is the Jacobian matrix of the error function, e is the error vector between the ANN output and the target output, μ is the learning parameter, and III is the identity matrix. This training method provides fast convergence and improved stability during offline learning.

F. Closed-Loop ANN Speed Controller

After training, the ANN is incorporated into the closed-loop speed control system of the BLDC motor as

$$\omega^*(t) \rightarrow [e(t), \Delta e(t)] \rightarrow ANN \rightarrow u(t) \rightarrow VSL/BLDCMotor \rightarrow \omega(t) \quad (38)$$

where ω∗(t) is the reference speed, [e(t), Δe(t)] are the ANN inputs, u(t) is the control output generated by the network, and ω(t) is the actual motor speed.

In this configuration, the ANN continuously adjusts the control signal according to the speed tracking error, thereby ensuring fast dynamic response, minimum overshoot, reduced steady-state error, and improved robustness against supply and load disturbances.

G. BLDC Motor Speed Dynamics

The mechanical dynamics of the BLDC motor can be represented by

$$T_e - T_L = J\frac{d\omega}{dt} + B\omega \quad (39)$$

where Te is the electromagnetic torque, TL is the load torque, J is the moment of inertia, B is the viscous friction coefficient, and ω is the rotor speed.

The electromagnetic torque is proportional to the phase current and is given by

$$T_e = K_t i \quad (40)$$

where Kt is the torque constant and i is the motor current. By controlling the inverter switching through the ANN-generated signal, the motor current and developed torque are regulated, which in turn controls the rotor speed.

VI. Results and Discussion

A. Performance Evaluation and Discussion of the Proposed System

The simulation results, as shown in Figure 8, demonstrate the dynamic behavior of the photovoltaic (PV) system when operating circumstances are disturbed or changed. The PV voltage (Vpv) is almost constant at around 300 V from 0 to 0.5 seconds, showing that the system is in a steady-state condition when it first starts up. while both the irradiance and the load remain constant, the PV array is most stable while running close to its ideal operating point, which might be under maximum power point tracking (MPPT) management. This region's lack of substantial swings proves that the converter and control approach are successfully regulating the output. But then, after about half a second, the PV voltage drops dramatically, going from around 300 V to roughly 150 V. This sudden shift suggests an interference, which may be caused by a number of things including a sudden shift in the load, changes in solar irradiation, or adjustments to the DC-DC converter's duty cycle. The voltage does not instantly level out after this dip; rather, it keeps going downhill until it finds a comfortable 120-130 V range. This slow decline might be an indication that the system is trying to find a new equilibrium point and is going through a temporary adjustment phase. The system has likely moved to a new working zone, maybe distant from its original maximum power point, if the final stabilized voltage is less than the starting value. This understanding of the system's dynamics is reinforced by the current waveform (Ib). As is typical of power electronic converter switching behavior, the current displays rather minor amplitude high-frequency oscillations before 0.6 seconds. Normal converter functioning is indicated by these oscillations, which are usually induced by pulse-width modulation (PWM) switching of semiconductor components. It seems like the current is focused around a tiny average value, which means that under stable circumstances, there is balanced energy transfer. The current waveform displays noticeable transient spikes around 0.6 seconds, just after the voltage disturbance, with peaks reaching 30-35 A. These spikes show the converter's rapid reaction to the unexpected voltage decrease; they indicate an increase in current as the system tries to make up for the difference. When operating circumstances change quickly, energy storage components like capacitors and inductors cause transient overshoots, which is a common occurrence in power electronic systems. The current waveform exhibits less oscillatory activity and becomes less dense in terms of switching frequency after this transient event, suggesting that the system is stabilizing. In tandem with the reduced voltage level shown in the PV output, the current amplitude seems to diminish and enter a new steady-state pattern. Although it may have reached a different equilibrium point, this indicates that the control system has effectively adjusted to the new operating state. The findings show that the system reacts dynamically to disturbances, going through a staggered stabilization phase after a distinct transient phase with

voltage dips and current spikes. The voltage and current responses clearly show the interaction between the control mechanism, the DC-DC converter, and the PV source. Although the system does reach stability, the existence of large transients suggests that the control technique should be improved to decrease overshoot and increase reaction time. These results show that PV-based power systems need strong control architecture to keep performing at their best and to reduce the effect of disturbances as much as possible.

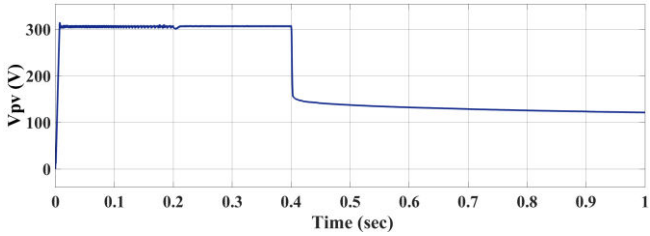

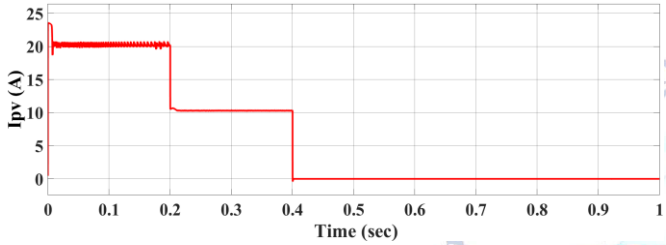

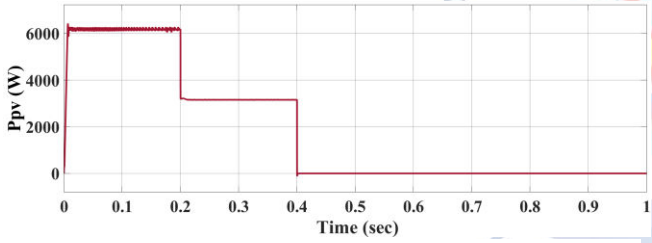

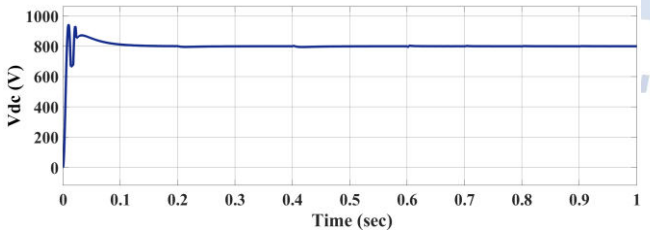

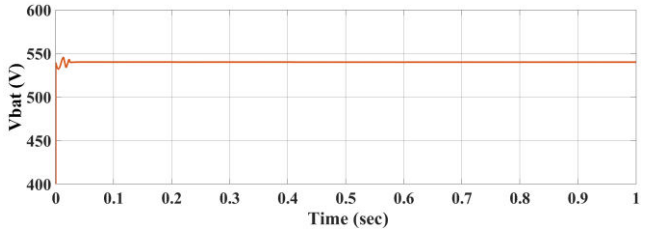

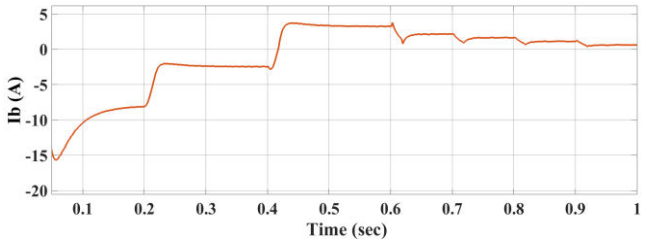

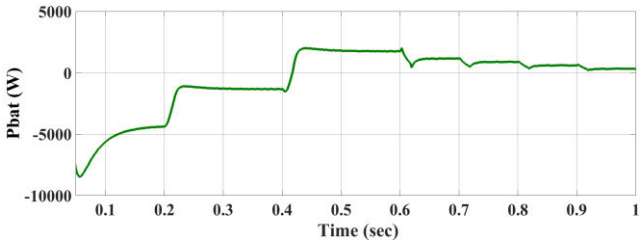

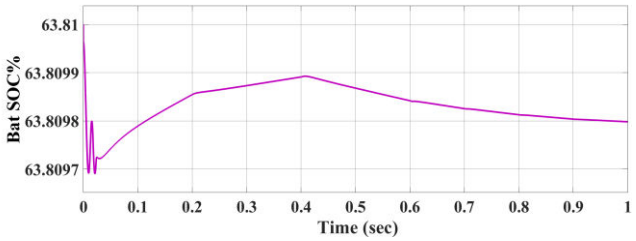

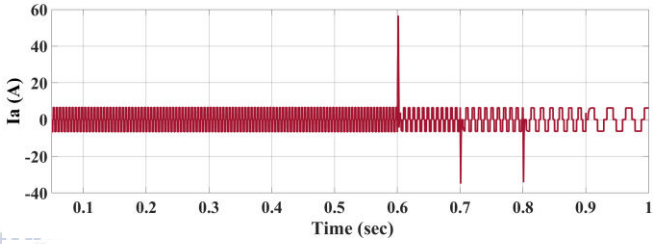

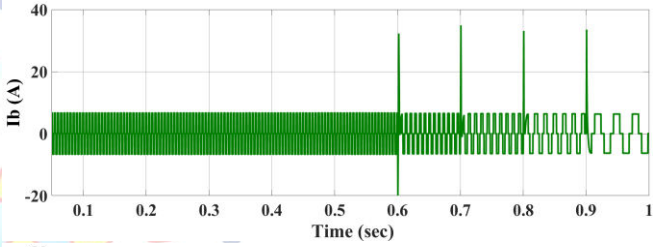

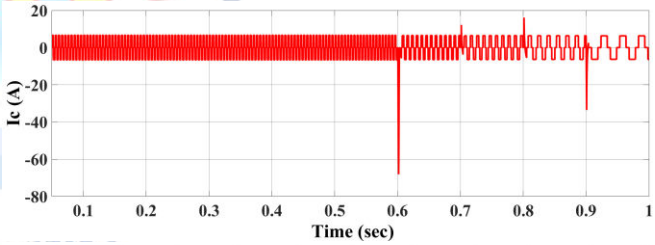

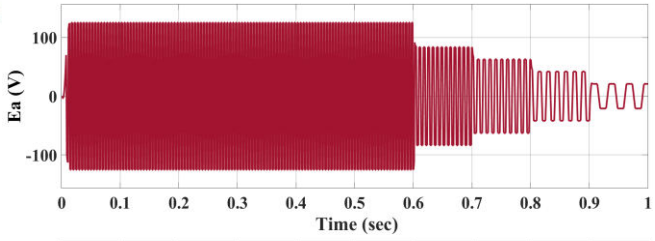

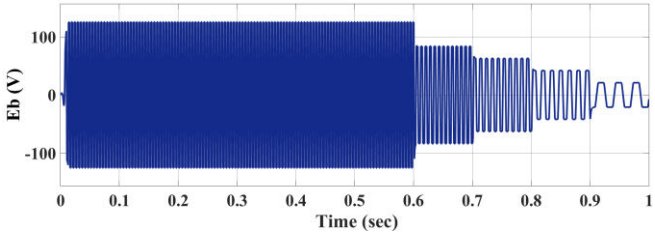

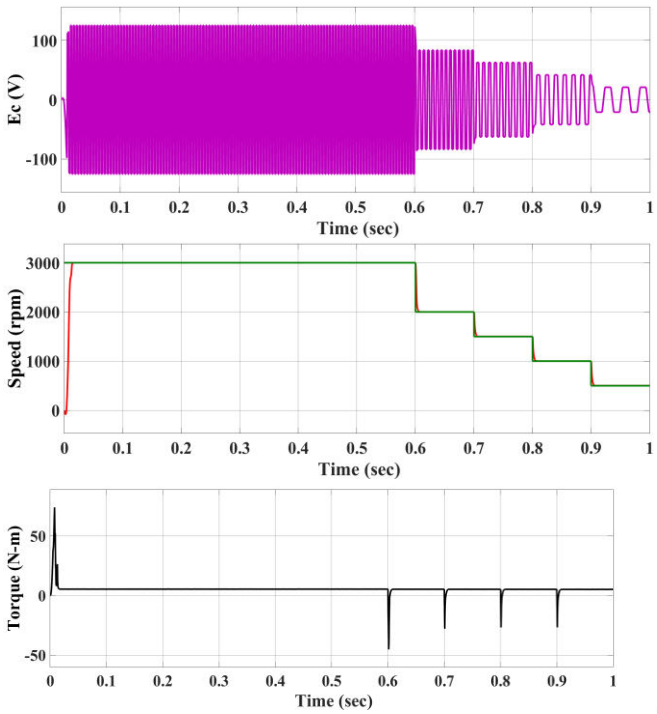

Fig.8 Simulation Results of proposed method ANN controlled BLDC motor Drive system

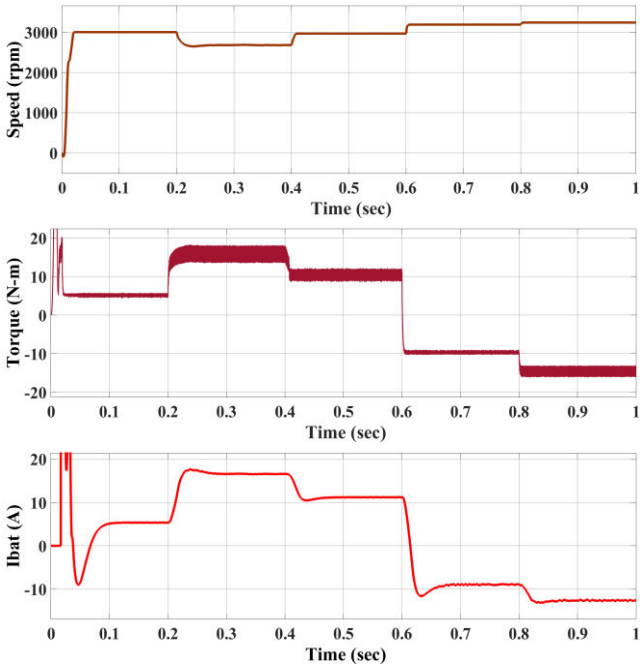

Fig.9 Simulation Results of Regenerative Braking Operation of PMBLDC Motor

B. Motoring and Regenerative Braking Operation of PMBLDC Motor

The simulation results demonstrate the effective operation of the PMBLDC motor under both motoring and regenerative braking modes. During the initial period, the motor operates in motoring mode, where the electromagnetic torque is positive, and electrical energy from the source is converted into mechanical energy to drive the load. In this mode, the speed increases smoothly and remains regulated as per the reference, while the battery supplies power to the motor. As the operating condition changes, the system transitions to regenerative braking mode, where the torque becomes negative. In this region, the motor behaves as a generator, converting the mechanical energy of the rotating system into electrical energy. This recovered energy is fed back to the battery, as indicated by the reversal of battery current direction. The speed decreases in a controlled manner during braking, ensuring stable operation without abrupt changes. The smooth transition between motoring and generating modes confirms the effectiveness of the proposed control strategy in enabling efficient energy utilization and reliable regenerative braking for LEV applications.

VI. CONCLUSION

This paper presented the design and implementation of an ANN-assisted adaptive speed controller for a position-sensorless PMBLDC motor drive with regenerative braking for LEV applications. The proposed system successfully eliminates the need for mechanical position sensors by employing a back EMF-based estimation technique, thereby reducing system cost and improving reliability. The integration of an Artificial Neural Network in the speed control loop enhances the overall performance of the drive by effectively handling nonlinearities, parameter variations, and external disturbances. The ANN-based controller demonstrates improved speed tracking capability with reduced steady-state error and faster dynamic response compared to conventional control methods. The incorporation of an adaptive delay compensation mechanism further improves the accuracy of sensorless operation by minimizing commutation delays. In addition, the regenerative braking strategy enables efficient recovery of kinetic energy during deceleration, contributing to improved energy efficiency and extended battery life, which are critical requirements for LEV applications. Simulation and experimental results validate the effectiveness of the proposed approach under varying operating conditions, showing enhanced robustness, stability, and energy utilization. Overall, the

proposed system provides a reliable, efficient, and intelligent solution for PMBLDC motor drives in light electric vehicles, making it a promising candidate for future energy-efficient transportation systems.

Conflict of interest statement

Authors declare that they do not have any conflict of interest.

REFERENCES

[1] IEA, "World Energy Outlook 2023", International Energy Agency, 2023.

[2] REN21, "Renewables 2023 Global Status Report", Renewable Energy Policy Network, 2023.

[3] A. Luque and S. Hegedus, Handbook of Photovoltaic Science and Engineering, Wiley, 2011.

[4] B. Parida, S. Iniyan, R. Goic, "A review of solar photovoltaic technologies," Renewable and Sustainable Energy Reviews, vol. 15, no. 3, 2011.

[5] G. Masson et al., "Global Market Outlook for Solar Power 2022-2026", SolarPower Europe.

[6] B. Kroposki et al., "Achieving a 100% Renewable Grid," IEEE Power & Energy Magazine, 2017.

[7] S. Mekhilef, R. Saidur, A. Safari, "A review on solar energy use in industries," Renewable and Sustainable Energy Reviews, 2011.

[8] MathWorks, "MATLAB Simulink Documentation," The MathWorks Inc., 2024.

[9] S. Jain and V. Agarwal, "Comparative study of maximum power point tracking techniques for solar PV systems using MATLAB," IEEE Transactions on Power Electronics, 2007.

[10] H. Patel and V. Agarwal, "Maximum power point tracking scheme for PV systems using single-stage inverter topology," IEEE Transactions on Energy Conversion, 2008.

[11] N. Femia et al., "Optimization of perturb and observe MPPT algorithm," IEEE Transactions on Power Electronics, 2005.

[12] T. Esram and P. Chapman, "Comparison of photovoltaic array maximum power point tracking techniques," IEEE Transactions on Energy Conversion, 2007.

[13] M. A. Elgendy et al., "An improved incremental conductance MPPT algorithm," IEEE Transactions on Sustainable Energy, 2013.

[14] N. Pandiarajan, Ranganath Muthu, "Mathematical modeling of PV module with Simulink," International Conference on Electrical Energy Systems, 2011.

[15] N. Mohan, Power Electronics: Converters, Applications and Design, Wiley, 2003.

[16] J. F. Gieras, M. Wing, Permanent Magnet Motor Technology, CRC Press, 2002.

[17] C. Xia, Permanent Magnet Brushless DC Motor Drives and Controls, Wiley, 2012.

[18] Y. Chen and K. T. Chau, "An overview of energy management in hybrid electric vehicles," Energy Conversion and Management, 2006.

[19] S. S. Williamson, A. K. Rathore, "Brushless DC motor drive with power factor corrected front-end converter," IEEE Transactions on Industrial Electronics, 2010.

[20] B. Singh et al., "Grid interfacing of renewable energy sources with power quality improvement," IEEE Transactions on Industrial Electronics, 2011.

[21] Y. Yang, F. Blaabjerg, "Power control strategies for grid-connected PV inverters with enhanced functionality," Energies, 2015.

[22] M. Islam, S. Mekhilef, "Power quality enhancement of grid-connected PV system," Energy Conversion and Management, 2014.

[23] A. Q. Huang, M. L. Crow, et al., "The future renewable electric energy delivery and management (FREEDM) system," Proceedings of the IEEE, 2011.

[24] S. A. Kalpande, P. P. Bedekar, "MPPT based solar water pumping system using BLDC motor," International Journal of Engineering Research and Technology, 2016.

[25] K. Karki et al., "Performance evaluation of grid-connected PV system in MATLAB/Simulink," IEEE International Conference on Power Electronics, 2019.

[26]